Accuracy and precision of navigated transcranial magnetic stimulation

Nieminen, Aino E.

2022-12-01

Nieminen , A E , Nieminen , J O , Stenroos , M , Novikov , P , Nazarova , M , Vaalto , S , Nikulin , V & Ilmoniemi , R J 2022 , ' Accuracy and precision of navigated transcranial magnetic stimulation ' , Journal of Neural Engineering , vol. 19 , no. 6 , 066037 . https://doi.org/10.1088/1741-2552/a

http://hdl.handle.net/10138/352944
https://doi.org/10.1088/1741-2552/aca71a

Accuracy and precision of navigated transcranial magnetic stimulation

Journal of Neural Engineering

PAPER

Accuracy and precision of navigated transcranial magnetic stimulation

Aino E Nieminen[1,2], **Jaakko O Nieminen**[1,*], **Matti Stenroos**[1], **Pavel Novikov**[1,3], **Maria Nazarova**[1,3,4], **Selja Vaalto**[1,5], **Vadim Nikulin**[3,6] **and Risto J Ilmoniemi**[1]

[1] Department of Neuroscience and Biomedical Engineering, Aalto University School of Science, Espoo, Finland
[2] AMI Centre, Aalto NeuroImaging, Aalto University School of Science, Espoo, Finland
[3] Centre for Cognition and Decision Making, Institute for Cognitive Neuroscience, National Research University Higher School of Economics, Moscow, Russia
[4] Athinoula A. Martinos Center for Biomedical Imaging, Massachusetts General Hospital, Charlestown, MA, United States of America
[5] HUS Diagnostic Center, Clinical Neurophysiology, Clinical Neurosciences, University of Helsinki and Helsinki University Hospital, Helsinki, Finland
[6] Department of Neurology, Max Planck Institute for Human Cognitive and Brain Sciences, Leipzig, Germany
[*] Author to whom any correspondence should be addressed.

E-mail: jaakko.nieminen@aalto.fi

Keywords: transcranial magnetic stimulation, TMS, neuronavigation, accuracy, precision, coregistration

Supplementary material for this article is available online

OPEN ACCESS

RECEIVED
25 April 2022

REVISED
7 September 2022

ACCEPTED FOR PUBLICATION
29 November 2022

PUBLISHED
16 December 2022

Abstract

Objective. Transcranial magnetic stimulation (TMS) induces an electric field (E-field) in the cortex. To facilitate stimulation targeting, image-guided neuronavigation systems have been introduced. Such systems track the placement of the coil with respect to the head and visualize the estimated cortical stimulation location on an anatomical brain image in real time. The accuracy and precision of the neuronavigation is affected by multiple factors. Our aim was to analyze how different factors in TMS neuronavigation affect the accuracy and precision of the coil–head coregistration and the estimated E-field. *Approach.* By performing simulations, we estimated navigation errors due to distortions in magnetic resonance images (MRIs), head-to-MRI registration (landmark- and surface-based registrations), localization and movement of the head tracker, and localization of the coil tracker. We analyzed the effect of these errors on coil and head coregistration and on the induced E-field as determined with simplistic and realistic head models. *Main results.* Average total coregistration accuracies were in the range of 2.2–3.6 mm and 1°; precision values were about half of the accuracy values. The coregistration errors were mainly due to head-to-MRI registration with average accuracies 1.5–1.9 mm/0.2–0.4° and precisions 0.5–0.8 mm/0.1–0.2° better with surface-based registration. The other major source of error was the movement of the head tracker with average accuracy of 1.5 mm and precision of 1.1 mm. When assessed within an E-field method, the average accuracies of the peak E-field location, orientation, and magnitude ranged between 1.5 and 5.0 mm, 0.9 and 4.8°, and 4.4 and 8.5% across the E-field models studied. The largest errors were obtained with the landmark-based registration. When computing another accuracy measure with the most realistic E-field model as a reference, the accuracies tended to improve from about 10 mm/15°/25% to about 2 mm/2°/5% when increasing realism of the E-field model. *Significance.* The results of this comprehensive analysis help TMS operators to recognize the main sources of error in TMS navigation and that the coregistration errors and their effect in the E-field estimation depend on the methods applied. To ensure reliable TMS navigation, we recommend surface-based head-to-MRI registration and realistic models for E-field computations.

1. Introduction

Transcranial magnetic stimulation (TMS) allows one to activate cortical neurons noninvasively [1]. A coil placed over the scalp generates a rapidly changing magnetic field, which induces an electric field (E-field) in the brain. The stimulation can be targeted at desired locations in the cortex with image-guided neuronavigation systems, which display the estimated location of the induced E-field maximum (navigation target) [2] on an anatomical brain image in real time [3–6]. Some navigation systems also show the direction and strength of the induced E-field at the location of the target [5]. Navigation systems include a tracking unit (often optical or electromagnetic) to follow the subject's head and the placement of the coil. The obtained position information is combined with an anatomical head image and with a 3D model of the coil in a process called coregistration to present all the information in the same coordinate system.

Neuronavigation enables accurate and precise stimulation targeting [7]. In this context, *accuracy* is a measure of the typical difference between the estimated stimulation site (or direction or E-field intensity) indicated by the neuronavigation system and the ground truth. On the other hand, *precision* is a measure of variation of the estimated target if the same navigation target were stimulated multiple times within a single session or in multiple sessions. Improved targeting precision enhances the repeatability of motor evoked potentials [8, 9] and TMS-evoked potentials measured with electroencephalography [10, 11]. Navigated TMS (nTMS) enables reliable mapping of cortical functions in motor [12–14] and speech areas [15, 16], for example, prior to neurosurgery. In addition, accurate and precise targeting is expected to increase the efficacy of treatment of various brain disorders [17–20].

Although neuronavigation increases the reliability of targeting, the methods are not perfect. Tracking the reference markers attached to the head, the coil, and the digitizer tool involves errors, which are often in the sub-millimeter range [21]. The coregistration process is affected by several additional error sources: selection of matching points from the 3D images, head, and coil, registration algorithms applied, and imperfections in the anatomical head image or the coil model [4, 22, 23]. Moreover, the head or coil tracker (reference frame) may move during a TMS session [4]. These errors lead to errors in the perceived relative placement of the head and the coil. In addition, there are uncertainties in defining the E-field on the cortex due to errors and simplifications in head segmentation and in the computational models [4, 5, 24, 25]. The simplest model applied is called line navigation, which assumes the E-field maximum to be at the location where the coil normal that passes through the coil center intersects the cortex [3]. This approach has been reported to be inaccurate especially with coil placements that are not tangential to the scalp surface [26]. Current E-field-navigated systems calculate the induced E-field with a spherical head model [27], fitting the sphere to the subject's head globally or locally [28]. More realistic models based on finite and boundary element methods (BEM) for E-field calculations with computation times allowing real-time navigation have been suggested [24, 29, 30]. Even the most realistic E-field computations, however, entail inaccuracies due to, e.g. uncertain conductivity values of the head [31], effects of head image segmentation [32, 33], brain shift between head postures [34], and simplifications, approximations, and limited level of detail in coil models [24, 35].

A few studies have reported measures for the accuracy and precision of TMS navigation systems [4, 5, 36, 37]. Ruohonen and Hannula [4, 5] report the accuracies of estimated peak E-field locations for a commercial system. Schönfeldt-Lecuona *et al* [36] present experimentally characterized differences for digitized landmark positions within and between TMS sessions. Souza *et al* [37] show measured accuracies and precisions for coil location and orientation. Some results in the context of image-guided neurosurgery regarding the accuracy and precision of tracker localization and the head-to-MRI registration [38, 39] are applicable also to TMS navigation. Currently available TMS navigation systems rely on various technological and methodological choices that make the accuracy and precision vary across systems. Moreover, we are unaware of earlier studies investigating the accuracy and precision of the estimated orientation and strength of the induced E-field, which are important parameters affecting brain activation [40].

With comprehensive simulations, we evaluated the accuracy and precision of currently available and most common TMS navigation methods. Our analysis provides the magnitude and spatial distributions of the errors related to TMS coregistration and the E-field estimation. It will help TMS users understand how different parts of the navigation systems affect the total error in locating the head and the coil. In addition, we show how these errors translate into the cortical navigation target, including the location of the estimated stimulation site as well as the orientation and strength of the induced E-field.

2. Methods

We carried out the simulations with two head models. The first one (Subject 1) represented a 36-year-old healthy male subject (head circumference 56 cm), who signed a consent form before participating in an MRI session. The study was approved by the ethical committee of the Hospital District of Helsinki and Uusimaa and was carried out in accordance with the Declaration of Helsinki [41].

For Subject 1, we acquired a T1-weighted MRI with fat suppression and a T2-weighted image as suggested by Nielsen *et al* [32], both with cubic 1 mm^3 voxels. The MRIs were scanned with a 3T Magnetom Skyra device (Siemens Healthcare GmbH, Germany). The second head model (Subject 2) representing a young healthy male was made from the fat-suppressed T1- and T2-weighted MRIs of 'Ernie' dataset of the SimNIBS software (https://simnibs.github.io/simnibs/build/html/dataset.html). All the simulations and analysis were performed with Matlab (The MathWorks, Inc., USA).

2.1. Head image segmentation

The head structures were segmented with the SimNIBS *headreco* pipeline [32], yielding meshes for the boundaries of scalp, skull, and cortex. The boundary meshes were downsampled and smoothed, resulting in pial, inner skull, outer skull, and scalp surfaces with 21 949, 4501, 4201, and 2901 vertices (3.5, 4.4, 6.0, and 7.5 mm mean vertex spacings), respectively, for Subject 1 and with 21 973, 4501, 4193, and 2901 vertices (3.5, 4.6, 6.5, and 8.2 mm mean vertex spacings), respectively, for Subject 2. The E-field computations were made on the left hemisphere on a cortical surface situated about 1.5 mm below the pial surface (1 mm mean vertex spacing).

2.2. Coregistration errors

Coregistration errors are errors in the estimation of the relative placement of the head and the coil. We estimated the coregistration errors with simulations, as done, e.g. in the field of neurosurgery navigation [42]. In the simulations, we assumed that the tracking unit can identify the locations of the head and coil trackers regardless of their placement. The steps in the registration and tracking processes are demonstrated in figure 1. As there are two common ways to perform the head-to-MRI registration, landmark-based and surface-based approaches, we studied both.

The first registration method, landmark-based registration, relies on matching sets of at least three landmark points selected from both the MRI and the physical head (see figure 1(B) top). For that, we manually selected three landmark points from the nodes of the scalp mesh: one point from each ear and the nasion landmark from the nose bridge. To induce the human error in selecting the MRI landmarks, as the selected landmarks may differ from the intended landmarks, we added isotropic 3D Gaussian displacements with a mean absolute error of 1.4 and 1.3 mm to the node points representing the ear landmarks and the nasion landmark, respectively. Similarly, we mimicked the inaccuracies in the localization of the tip of the digitizer tool and the human error in selecting the corresponding landmarks from the physical head with isotropic 3D Gaussian errors with mean absolute values of 2.4 mm (ears) and 1.8 mm (nasion). These values for the mean landmark errors are averages of the empirical results of Shamir *et al* [43] and Omara *et al* [44]. The two noisy sets of the landmarks were registered with least-squares minimization [45] (Matlab implementation: http://faculty.cooper.edu/mili/Calibration/RT/umeyama.m). The obtained transformation matrix gives the error due to the landmark-based registration.

The second registration method, surface-based registration, is based on first performing the landmark-based registration and then digitizing points on the scalp and matching the point cloud to the scalp mesh derived from the MRI. To simulate this digitization process, we divided the scalp mesh into 21 patches, as it is important to digitize points all over the scalp to ensure a good registration. On each simulation run, we randomly picked one scalp mesh node from each patch, and translated the point 0–5 mm (uniform distribution) to a random direction along the scalp (see figure 1(B) bottom). The random translation of the points along the scalp made the simulation more realistic, as the digitized points could be any points on the scalp, not only the mesh vertices. We added isotropic 3D Gaussian displacements with a mean absolute error of 0.5 mm to these digitized points to mimic the errors due to the tracking of the digitizer pen, the soft skin, and the control of the digitizer by the human operator. The digitized pointset was registered to the scalp mesh with the iterative closest point algorithm [46] implemented in the *pcregistericp* Matlab function with the point-to-plane option. The transformation obtained from the landmark-based registration served as an initial guess for the surface-based registration.

In both registration methods, MRI deformations (the same for each run; figure 1(A)) were simulated by shrinking the scalp mesh towards the origin of the MRI image with displacements of $0.015r^2 + 0.0001$, where r is the distance from the origin in meters. This deformation approximately matches the average magnitude of the residual MRI deformations after 3D distortion correction measured by Torfeh *et al* [47]. In addition, shifts of the ear landmarks due to hearing protection and support pillows during MRI scanning were estimated with isotropic 3D Gaussian displacements with an average absolute error of 1.0 mm (the error varies from run to run).

Errors in the head tracker localization were simulated by placing a triplet of tracker markers (spacings: 42, 50, and 65 mm) above the forehead (see figure 1(C)) and adding isotropic 3D Gaussian noise with 0.2 mm mean displacement ([48]; a typical value for optical tracking systems) to the tracker markers. Then, the transformation between the original and noisy marker triplets was determined with least-squares minimization applied also in the landmark-based head-to-MRI registration. The movement of the head tracker (due to, e.g. sliding down along the skin or up–down movements of the forehead skin)

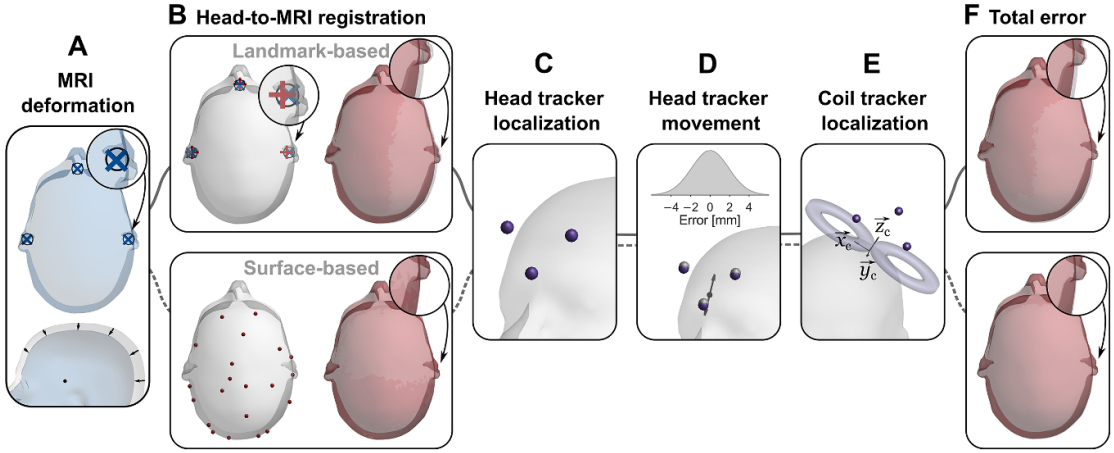

Figure 1. Example simulation run of the coregistration errors with Subject 1. (A) Simulated MRI deformation: shrunken head model (blue surface) and erroneous MRI landmarks (blue crosses; ground truth landmarks as black circles). The right ear area is enlarged. The bottom figure illustrates an exaggerated deformation. (B) Head-to-MRI registration. Top: landmark-based registration between three erroneous MRI landmarks (blue crosses) and three erroneous landmark points digitized from the physical head (red plusses). Bottom: registration between the scalp mesh (gray surface) and the erroneous digitized physical scalp points (red spheres). The right ear areas are enlarged. (C) Head tracker localization: head tracker markers above the forehead are visualized as purple spheres. A small error in their localization is added in the simulations. (D) Head tracker movement is simulated by translating all head tracker markers up or down along the forehead surface (gray arrows) with a distance sampled from a Gaussian distribution (shaded gray probability density curve) leading to a shift between the true and expected head placements. (E) Small errors in tracking the three coil markers (purple spheres) lead to a small transformation between true and navigated coil placements. The coordinate axes ($\vec{x}_c, \vec{y}_c, \vec{z}_c$) of the figure-of-eight coil are marked as dark gray arrows. (F) Total coregistration error ((A)–(E) combined) on one simulation run (landmark-based registration on the top, surface-based on the bottom). In (A) and (F), the gray surfaces indicate where the navigation system assumes the head (and coil) is placed. The red surfaces demonstrate the error in the relative placement of the head and the coil due to inaccuracies in the tracking process.

was mimicked by translating the tracker markers up and down along the scalp surface on the forehead (see figure 1(D)). The added random displacements were sampled from a 1D normal distribution with 1.5 mm mean absolute error. The error in the coil tracker localization was simulated similarly to the error in the head tracker localization, except that the coil marker triplets were moved with the coil model around the head.

The described simulations of the errors in the registration and tracking processes were repeated 10 000 times. The effects of different error sources were simulated separately with no errors in the other steps of the tracking process. In addition, the total coregistration errors were computed by combining all the simulated error transformations in one simulation run. The error metrics were separated into accuracy and precision. The accuracy was computed as the mean difference between the shown placement of the head and the coil (location/orientation) and N simulated displaced locations/orientations due the coregistration errors:

$$\text{accuracy} = \frac{1}{N}\sum_{n=1}^{N} A_n \,. \tag{1}$$

When computing location accuracy, $A_n = \left|\vec{p}_{\text{shown}} - \vec{p}_{n,\text{displaced}}\right|$ was the Euclidean distance between the 3D location $\vec{p}_{\text{shown}}$ shown by the navigation system and the displaced location $\vec{p}_{n,\text{displaced}}$. For orientation accuracy, $A_n = \measuredangle(\vec{d}_{\text{shown}}, \vec{d}_{n,\text{displaced}})$ was the angle between the shown orientation $\vec{d}_{\text{shown}}$ and the actual orientation $\vec{d}_{n,\text{displaced}}$. The precision was determined as the standard deviation of the differences between the N repeated erroneous head–coil placements (locations/orientations) and their mean:

$$\text{precision} = \sqrt{\frac{1}{N-1}\sum_{n=1}^{N} B_n^2} \,. \tag{2}$$

With location precision, $B_n = |\vec{p}_{n,\text{displaced}} - \vec{p}_{N,\text{average}}|$ was the distance between the displaced location $\vec{p}_{n,\text{displaced}}$ and the average displaced location $\vec{p}_{N,\text{average}}$ over N repetitions. With orientation precision, $B_n = \measuredangle(\vec{d}_{n,\text{displaced}}, \vec{d}_{N,\text{average}})$ was the angle between the displaced orientation $\vec{d}_{n,\text{displaced}}$ and the average displaced orientation $\vec{d}_{N,\text{average}}$. In addition, we computed the within-session precision, including errors in the tracker localization and the head tracker movement. The orientation errors were computed separately for the coil normal and tangents (average over six tangential directions from −90° to 60° with 30° steps, with 0° corresponding to the posterior–anterior direction).

Moreover, navigation systems usually provide a root-mean-square error (RMSE) after the head-to-MRI registration as a measure of the quality of the registration. We also computed such RMSEs with all simulation runs to compare them with the actual coregistration errors. With landmark-based registration, the RMSE was computed between the

registered landmark point sets. The RMSE after the surface-based registration was computed for the distances between the digitized points and the scalp surface mesh with the *pcregistericp* Matlab function.

2.3. Errors in E-field estimation

We investigated how the simulated coregistration errors (i.e. errors in the determination of the relative placement of the head and the coil) translate into errors in the estimated E-field maximum on the cortex. We calculated the peak E-field characteristics with five different methods: line navigation, two spherical models, and three realistically shaped models (see figure 2). In line navigation, we projected the coil center along the coil normal ($\vec{z}_c$) to the surface of the cortex with the fast triangle–ray intersection algorithm [49] (Matlab implementation: www.mathworks.com/matlabcentral/fileexchange/33073-triangle-ray-intersection). The intersection point represents the estimate for the peak E-field location, and the direction of the E-field was approximated as the direction of the coil ($\vec{y}_c$).

With the spherical model, we calculated the induced E-field in the cortex due to magnetic dipoles representing the TMS coil by applying the reciprocity principle [27, 50]. In this process, the magnetic field outside the spherically shaped head due to a current dipole on the cortex was computed with the analytical Sarvas formula [51]. We considered both globally and locally fitted spherical models. The global spherical head model was fitted by minimizing in the least-squares sense the distance between the spherical surface and the points of the whole inner skull surface. The local models were fitted to a patch of the inner skull surface below the coil: first, we projected the coil center to the inner skull surface and extracted the inner-skull points within a 3 cm radius from the projected point. Then, we fitted a sphere to that pointset in the least-squares sense with the radius of the sphere constrained to 3–30 cm. With the spherical models, we considered only valid field points, i.e. the cortical points that were deeper in the fitted sphere than the coil dipole closest to the origin of the fitted sphere.

With realistic models, the E-field was solved reciprocally using methods and tools described and verified in [24]. The dipole potentials needed in the reciprocal formulation were solved using the Galerkin BEM with linear basis functions, formulated with the isolated source approach [52, 53]. All coil-related computations were done directly in the cortical points using quick beta integrals and analytical formulas of [24] as implemented in the *hbftms_realtime* library that is publicly available at https://github.com/MattiStenroos/hbftms_realtime. The coil model is also available in that library. The simplest realistic model was the single-compartment model (1C BEM) that contains the intracranial space (conductivity 0.33 S/m), bounded by the inner skull surface. This model, originally introduced for magnetoencephalography in [54], has previously been suggested for fast TMS computations in [28]. The three-compartment model (3C BEM) comprises the intracranial compartment, skull, and scalp. Based on results of [28], it was expected to produce results very similar to the single-shell model. The four-compartment model (4C BEM) separates the intracranial space to cerebrospinal fluid and brain, thus introducing realistic gyral structure whose contribution to E-field amplitude and focality was demonstrated in [55]. The 4C model was in the between-methods comparisons of this study regarded as the reference model. The conductivity for the scalp and brain was 0.33 S/m, for cerebrospinal fluid 1.79 S/m, and for the skull 0.0041 or 0.0066 S/m with 3C or 4C BEMs, respectively.

Our coil model mimics a typical figure-of-eight coil with 42 magnetic dipoles [24]. The modeled coil was set tangentially with respect to the scalp surface at 21 locations on the left side of the head, the locations corresponding to electrode sites in a 10-10 electroencephalography montage. On each coil location, the coil model was rotated into six tangential directions (from $-90°$ to $60°$ with $30°$ steps, $0°$ in the posterior–anterior direction) with nine tilting angles ($0°$; $\pm5°$ and $\pm10°$ in both main tangential directions $\vec{x}_c$ and $\vec{y}_c$) resulting in $6 \times 9 = 54$ intended coil placements per location. Tilted coil models that would have intersected with the scalp were translated along the scalp normal from their original place until the coil model was outside the head, i.e. the coil dipoles were at least 6.5 mm above the scalp.

With each intended coil placement, the coil model was perturbed with 50 (out of 10 000) error transformations obtained from the coregistration error simulations. We considered only total coregistration errors and accepted only cases where the whole coil model was outside the head. The corresponding E-fields were calculated with the six described methods: line, local and global sphere, 1-, 3-, and 4-compartment BEM. With sphere and BEM methods, the E-field was computed in vertices of a densely-meshed cortical region of interest determined separately for each of the 21 coil locations. These regions of interest were defined using computations in a coarser cortex mesh: they represent areas in which any of the E-field computation methods produced field magnitudes larger than 80% of the corresponding E-field maximum for given unperturbed coil location, with any tangent or tilt directions. With line navigation, the peak E-field location was determined with a local dense mesh including the part of the cortex within 5 cm from the initial coil location. For each coil placement and E-field model, we extracted the location, direction, and strength (no strength for line navigation) of the peak E-field. In these calculations, the location of the peak E-field was defined as the center of gravity of the E-field exceeding 98% of the maximum E-field magnitude; the direction and strength

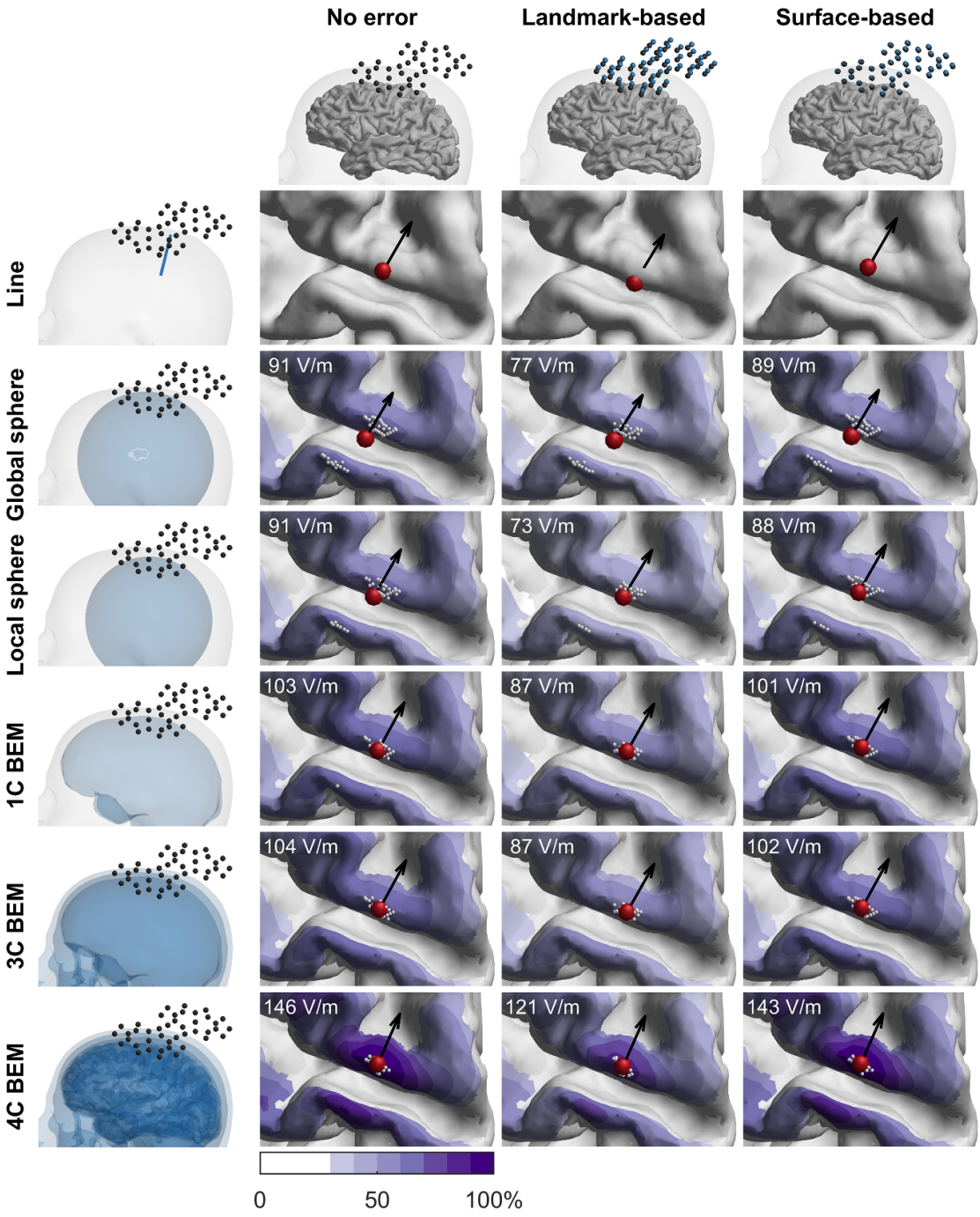

Figure 2. E-field estimation methods and examples of E-fields with coregistration errors with Subject 1 when the TMS coil is placed tangentially above the primary motor cortex. Illustrations of the E-field computation models on the left column. The second column shows the case with no error in the coregistration, the third column an example case of the total error with landmark-based registration, and the right column row an erroneous coregistration with surface-based registration. The purple isocolors indicate the E-field magnitude relative to the maximum E-field magnitude in the reference model without error (second column on the bottom row). The location, orientation, and magnitude of the E-field maximum are depicted with a red sphere, black arrow, and white text, respectively. The small gray spheres around the red sphere indicate the node points utilized to determine the peak E-field, i.e. nodes of the cortex mesh exceeding 98% of the E-field maximum in the corresponding case. In the left and top panels, the coil dipoles without error are visualized with black spheres and the erroneous ones with blue spheres (only on top row).

of the peak E-field were taken as averages within the corresponding region. The areas above 98% of the E-field maximum included on average 32, 29, 26, 27, and 12 vertices of the cortex mesh for the global sphere, local sphere, 1C, 3C, and 4C BEM methods, respectively.

The accuracies in the E-field navigation were determined with equation (1) as the mean differences in the location, orientation, and magnitude of the peak E-field without perturbations in the coil positioning, i.e. what the navigation system shows, and a reference, which is the actual E-field maximum due

to errors in the coil placement. We evaluated two different accuracy metrics. The first one was a within-method accuracy, in which the test and the reference results were all determined with the same computational method. In addition, we considered differences between different E-field methods, repeating the accuracy analysis with the most realistic 4C BEM model as reference. The precision was computed with equation (2) as the standard deviation of the absolute differences between the peak E-field location, orientation, and magnitude over the $N = 50$ erroneous coil placements and their corresponding mean. The magnitude errors were computed as absolute relative differences in percent. For line navigation, we obtained error metrics only for position and orientation. The error outcomes were averaged over coil directions and tilts on each of the 21 coil locations.

3. Results

3.1. Coregistration errors

The accuracy and precision maps on the scalp for Subject 1 are presented in figures 3 and 4. The corresponding results for Subject 2 are very similar and can be found in the supplementary material (supplementary figures S1 and S2). Figure 3 and supplementary figure S1 show that with the landmark-based registration, the limited accuracy of the registration process resulted in the relatively poor total navigation accuracy of 3.6 mm/1.2° for Subject 1 and 3.5 mm/1.1° for Subject 2; placements on top of the head were associated with the worst location accuracy of about 4 mm. With the surface-based registration, the navigation accuracy improved everywhere on the scalp; the total average accuracies were 2.2 mm/0.9° for Subject 1 and 2.3 mm/1.0° for Subject 2.

The precision maps are visualized in figure 4 and supplementary figure S2. The surface-based registration yielded better total precision (Subject 1: 1.2 mm/0.5°; Subject 2: 1.3 mm/0.6°) than the landmark-based registration (Subject 1: 1.7 mm/0.7°; Subject 2: 1.6 mm/0.6°). The total within-session precisions for both subjects were 1.1 mm and 0.2°. Figure 5 and supplementary figure S3 illustrate the relationship between the registration RMSE and the simulated total error.

3.2. E-field-navigation errors

The accuracy of the estimated target site on the cortex (E-field maximum) with different E-field computation methods is presented as scalp maps in figure 6 and supplementary figure S4 for Subjects 1 and 2, respectively. Average within-method accuracy was the poorest, about 5 mm, with line-navigated targeting combined with landmark-based registration; the accuracies of the sphere- and BEM-model-based targeting methods were better, being about half of that of the line-navigated option. When comparing the outcomes with the 4C-BEM model as a reference (between-methods comparison), the poorest accuracy of about 10 mm was observed with line navigation followed by spherical models (∼8 mm), 1C/3C BEMs (∼7 mm), and the reference model 4C BEM (∼2 mm). With within-method accuracies, surface-based registration led to on average 0.6 mm better accuracy than the landmark-based registration. In the between-methods comparison, such differences between the registration methods disappeared.

The precision maps of the estimated cortical target site are depicted in figure 7 and supplementary figure S5 for Subjects 1 and 2, respectively. Surface-based registration yielded on average 0.6 mm better precision than landmark-based registration. The errors occurring during a TMS session led to average precisions in the range of 0.7–2.2 mm. Among the targeting methods, the best precisions were with the 1C/3C BEMs and the global sphere.

The accuracies and precisions of the E-field directions and magnitudes for Subjects 1 and 2 are listed in table 1 and supplementary table S1 (accuracies), respectively, and table 2 and supplementary table S2 (precisions), respectively. Table 1 and supplementary table S1 indicate that the average within-method accuracies for direction/magnitude were in the range of 1.1°–4.8°/7.1%–8.5% for the landmark-based and 0.9°–4.2°/4.4%–6.0% for the surface-based registration. The between-method accuracies, excluding the reference model 4C BEM, worsened to 7.4°–14.8°/11.1%–24.8% and 7.3°–14.8°/11.7%–26.7% with the landmark- and surface-based registrations, respectively. Table 2 and supplementary table S2 show that with both registration methods, line navigation was the most precise with respect to direction (0.5°–0.6°) whereas the local sphere method had the poorest precision (2.3°–6.4°). Surface-based registration was associated with better E-field magnitude precision (1.6%–2.2%) than landmark-based registration (2.3%–3.3%).

4. Discussion

In this study, we simulated errors related to TMS navigation systems. The results do not correspond to any specific TMS navigation system, as the exact methods applied in commercial systems vary from system to system. Instead, our analysis considered one simulated realization of the general principles in tracker localization, registration process, and E-field estimation that are in some way implemented in most TMS navigation systems.

4.1. Coregistration errors

According to our simulations, the coregistration accuracy is generally 2–4 mm, depending on the position on the scalp (figure 3 and supplementary figure S1). The largest contributor to the coregistration error is the head-to-MRI registration process. The landmark-based registration results in considerably

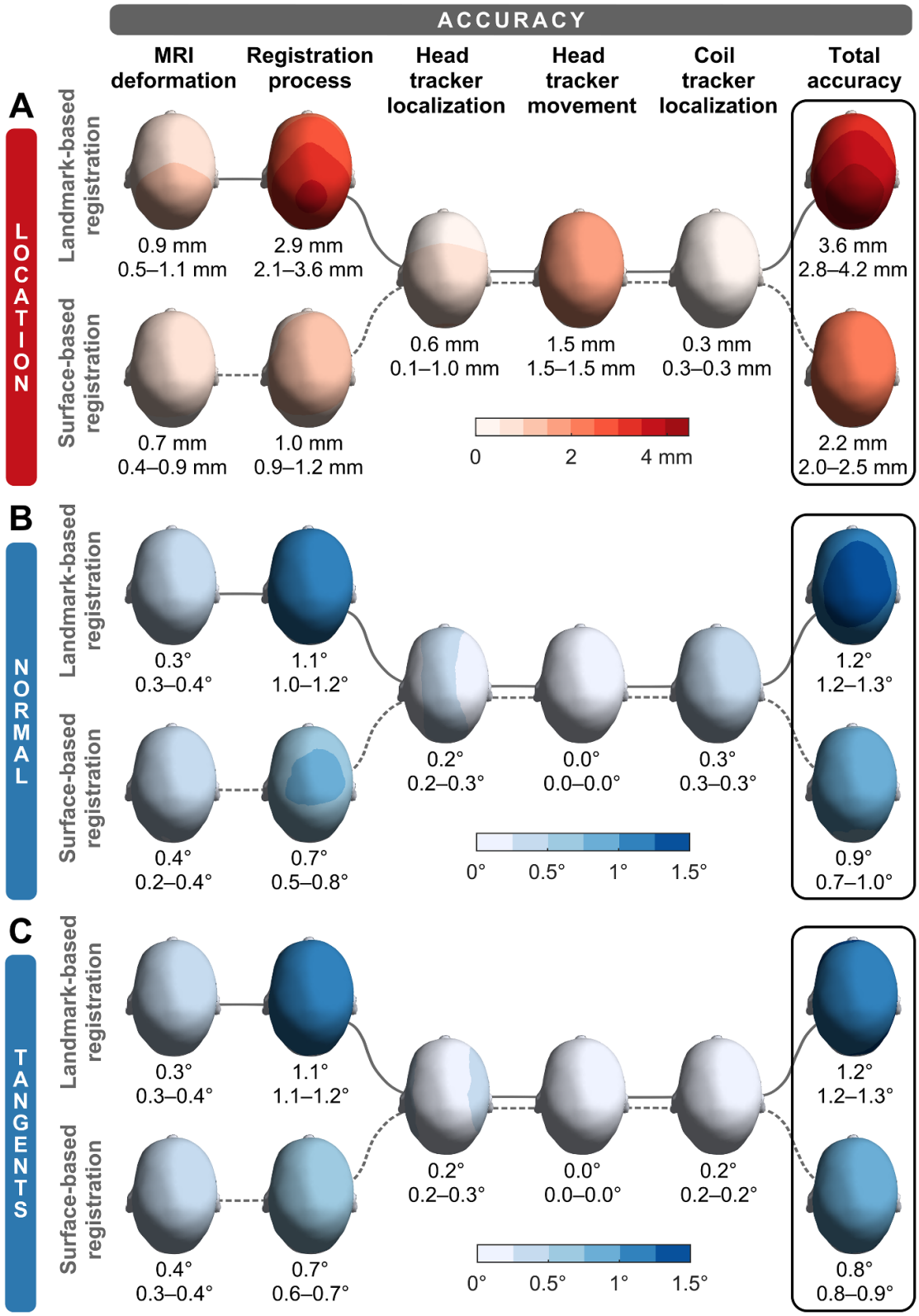

Figure 3. Accuracy of coregistration. Coregistration accuracy maps with Subject 1 for coil locations (A), coil normals (B), and coil tangent orientations (C), i.e. how much the actual coil location/direction differs from what is shown by the navigation system. The isocolors represent the mean absolute errors over 10 000 simulation runs. The values below each scalp distribution indicate the accuracy averaged over scalp points (upper line) and the range of the mean accuracies across scalp points (bottom line). The five leftmost columns show the accuracies of different parts of the navigation process and the rightmost column shows the total accuracy with all simulated error sources combined. The chain of accuracies is plotted separately for landmark-based (indicated with gray solid line) and surface-based (gray dashed line) registrations.

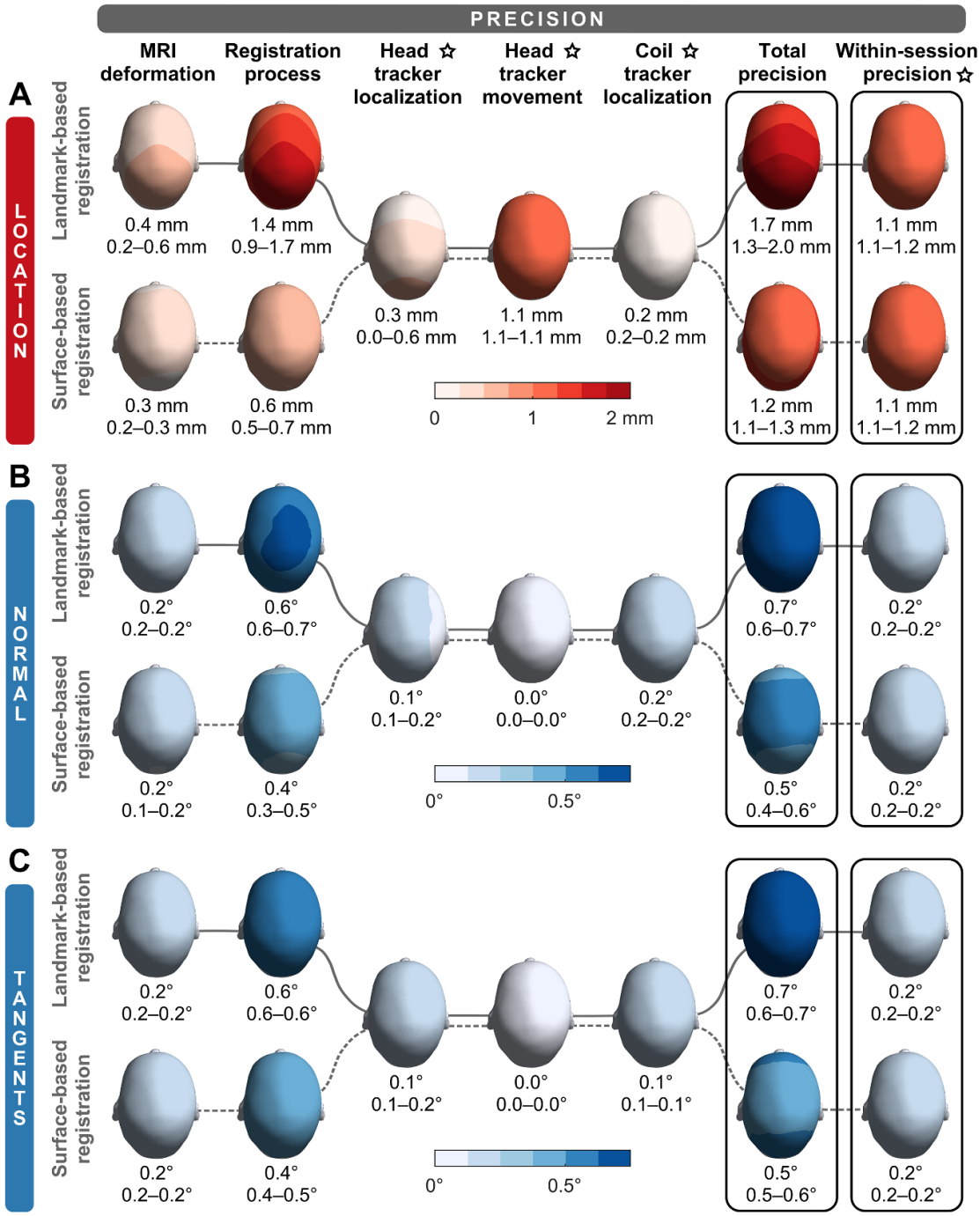

Figure 4. Precision of coregistration. Coregistration precision maps with Subject 1 for coil locations (A), coil normals (B), and coil tangent orientations (C). The isocolors represent the standard deviation over 10 000 simulation runs. The values below each scalp distribution indicate the precision averaged over scalp points (upper line) and the range of the mean precisions across scalp points (bottom line). The five leftmost columns show the precisions of different parts of the navigation process, the second rightmost column shows the total precision with all simulated error sources combined, and the rightmost column visualizes the within-session precision including uncertainties in elements that can change during one simulation session (head/coil tracker localization and head tracker movement; indicated with black stars). The chain of precisions is plotted separately for landmark-based (indicated with gray solid line) and surface-based (gray dashed line) registrations.

worse localization (∼3.5 mm) than the surface-based registration (∼2 mm) because the landmark-based registration utilizes fewer points for the registration and thus is more sensitive to errors of single points. The precision values are typically about half of the accuracy values (figure 4 and supplementary figure S2). The registration method affected the accuracy and precision of the coil orientation only moderately, with the average total accuracy and precision being about 1° and 0.5°, respectively. In navigation relying on the landmark-based registration, the largest location errors of about 4 mm on average were present on the back/top of the head and the smallest errors of about 3 mm on the frontal and temporal parts of the head. This was expected, as it is known that the errors increase further away from the landmark points [56].

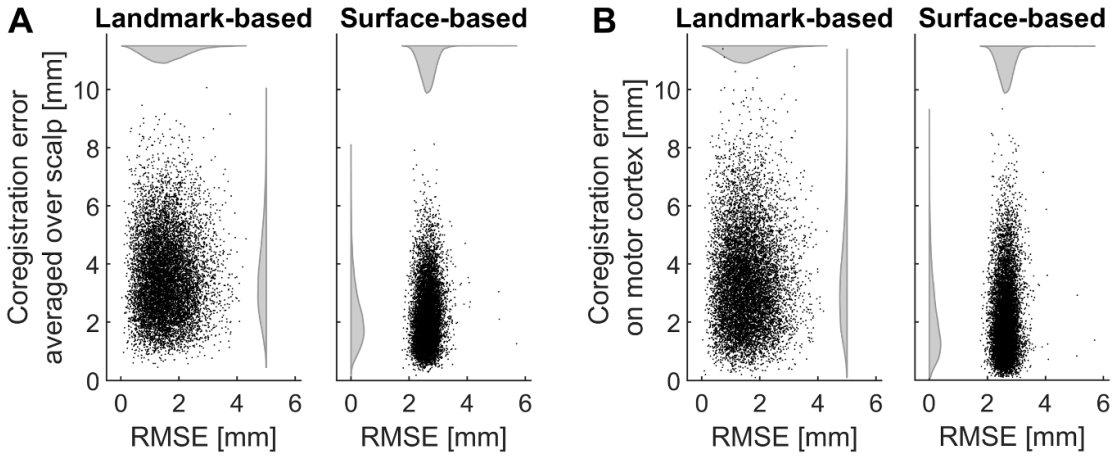

Figure 5. RMSE after registration (usually given by the navigation system) versus simulated total coregistration error averaged over scalp points (A) and on a scalp point above the motor cortex (B) with Subject 1. The black dots depict single simulation runs and the gray areas illustrate the marginal distributions. Note that RMSEs (horizontal axes) between left and right panels in (A) and (B) cannot be directly compared as they are computed differently (see the end of section 2.2). The data along vertical axes are comparable.

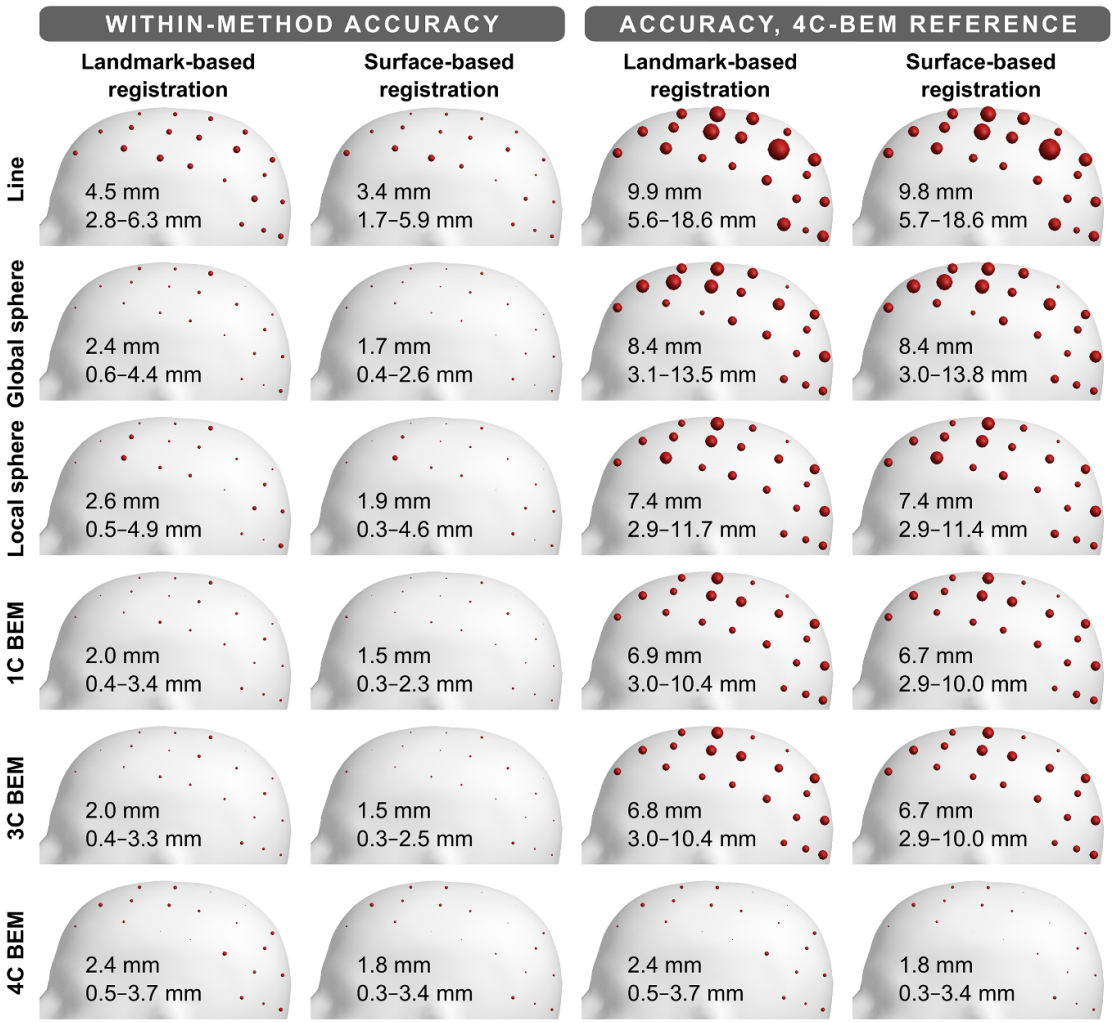

Figure 6. Accuracy of the peak E-field locations for different E-field methods (on different rows) with Subject 1. The first two columns visualize the accuracies within a method, whereas the two right-most columns present the accuracies when the most realistic model (4C BEM) was utilized as a reference. The diameter of the red spheres indicates the average accuracy of the peak E-field location (averaged over tangent directions, tilts, and error repetitions) when the coil was placed on the corresponding location on the scalp (21 locations). The values in each subplot describe the mean accuracy over all coil locations (upper line) and the range of the location-wise mean accuracies (bottom line).

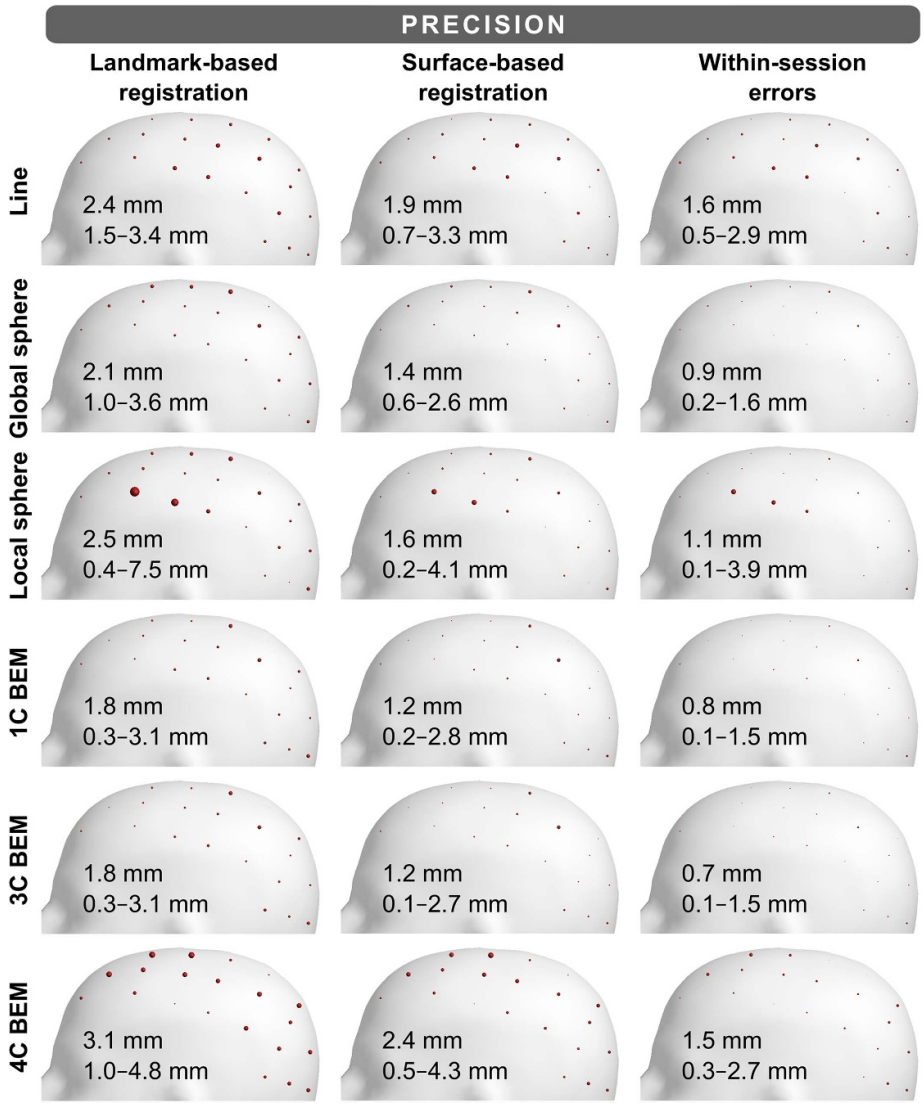

Figure 7. Precision of the peak E-field locations for different E-field methods (on different rows) with Subject 1. The first column visualizes the precisions when the registration is done with the landmark-based approach. The middle column illustrates the precisions with the surface-based registration. The right-most column presents the within-session precision. The diameter of the red spheres indicates the average precision of the peak E-field location (averaged over tangent directions, tilts, and error repetitions) when the coil was placed on the corresponding location on the scalp (21 locations). The values in each subplot describe the mean precision over all coil locations (upper line) and the range of the location-wise mean precisions (bottom line).

Table 1. Within-method accuracies and accuracies with the 4C BEM as a reference model for E-field directions and magnitudes with Subject 1. The accuracy values are reported separately for the different E-field (rows) and registration (columns) methods. The first value in each cell describes the mean accuracy over all 21 coil locations; the range of the location-wise mean accuracies is in the parenthesis.

		Within-method accuracy		Accuracy (4C BEM as a reference)	
	E-field method↓	Landmark-based registration	Surface-based registration	Landmark-based registration	Surface-based registration
Direction	Line navigation	1.2 (1.1–1.3)°	0.9 (0.8–1.0)°	9.4 (6.0–14.7)°	9.4 (5.8–14.4)°
	Global sphere	2.1 (1.0–3.8)°	1.5 (0.8–2.4)°	14.3 (8.0–24.4)°	14.3 (7.9–24.5)°
	Local sphere	2.8 (1.0–9.7)°	2.1 (0.6–8.3)°	8.8 (3.4–15.5)°	8.9 (3.4–16.0)°
	1C BEM	1.7 (0.8–3.3)°	1.3 (0.5–2.9)°	7.6 (3.2–11.7)°	7.6 (3.2–11.4)°
	3C BEM	1.6 (0.8–2.9)°	1.2 (0.5–2.4)°	7.6 (3.3–11.7)°	7.5 (3.3–11.4)°
	4C BEM	2.5 (1.2–4.1)°	1.9 (0.8–3.7)°	2.5 (1.2–4.1)°	1.9 (0.8–3.7)°
Magnitude	Line navigation	—	—	—	—
	Global sphere	8.3 (5.7–10.5)%	6.0 (3.0–9.0)%	14.4 (4.4–25.5)%	15.4 (3.7–26.2)%
	Local sphere	8.5 (5.2–12.9)%	5.8 (1.3–12.8)%	23.0 (11.9–39.1)%	24.6 (15.4–40.5)%
	1C BEM	8.1 (5.7–10.4)%	5.8 (2.2–9.3)%	16.0 (10.3–20.8)%	17.8 (13.3–22.6)%
	3C BEM	8.1 (5.6–10.3)%	5.8 (2.3–9.3)%	14.7 (9.2–19.0)%	16.5 (12.0–20.9)%
	4C BEM	8.0 (5.7–10.4)%	5.7 (2.1–9.9)%	8.0 (5.7–10.4)%	5.7 (2.1–9.9)%

Table 2. Precisions of E-field directions and magnitudes with Subject 1. Total precisions with the landmark- and surface-based registrations as well as the within-session precision are presented in different columns for each E-field method (rows). The first value in each cell describes the mean precision over all 21 coil locations; the range of the location-wise mean precisions is in the parenthesis.

		Precision		
	E-field method↓	Landmark-based registration	Surface-based registration	Within-session precision
Direction	Line navigation	0.6 (0.5–0.7)°	0.5 (0.4–0.6)°	0.2 (0.2–0.2)°
	Global sphere	1.5 (0.8–3.1)°	1.1 (0.7–2.3)°	0.6 (0.2–1.4)°
	Local sphere	3.7 (0.6–18.9)°	2.3 (0.4–12.3)°	1.8 (0.2–10.8)°
	1C BEM	1.4 (0.5–4.0)°	1.0 (0.4–3.0)°	0.6 (0.1–2.4)°
	3C BEM	1.3 (0.5–3.2)°	0.9 (0.4–2.2)°	0.6 (0.1–1.9)°
	4C BEM	2.6 (1.1–4.6)°	2.0 (0.6–4.1)°	1.3 (0.3–2.6)°
Magnitude	Line navigation	—	—	—
	Global sphere	2.7 (1.7–3.4)%	2.0 (0.9–2.9)%	1.8 (0.8–2.7)%
	Local sphere	3.3 (2.0–5.6)%	2.2 (0.9–4.7)%	1.8 (0.7–3.9)%
	1C BEM	2.6 (1.6–3.5)%	2.0 (0.9–2.9)%	1.7 (0.8–2.7)%
	3C BEM	2.6 (1.6–3.5)%	1.9 (0.9–2.9)%	1.7 (0.8–2.7)%
	4C BEM	2.8 (1.8–3.6)%	2.0 (0.9–3.0)%	1.7 (0.8–2.7)%

In addition, the accuracy and precision maps are quite symmetric in the left–right direction, although there are slight asymmetries likely due to minor anatomical asymmetry of the head models. We recommend using a surface-based registration process with points digitized all over the scalp whenever possible. The within-session precision could be best controlled by ensuring a stable head tracker.

The simulations were limited to two subjects, whose accuracy and precision maps were very similar. We expect that the error profiles would be congruent across a larger set of subjects, with the subject affecting mainly their scale: a smaller or a larger head would lead to smaller or larger errors, respectively. To confirm this, simulations with a larger subject group would be needed in the future. The obtained accuracy and precision maps were simulated with parameters taken from the literature when possible. There can, however, be large differences over operators (e.g. due to a varying level of carefulness) in selecting the points from the physical head and the MRI in the registration. Thus, in practice, the errors might be even larger than reported here. Moreover, the MRI deformations especially without gradient nonlinearity correction and head tracker movements may be larger in practice. In this work, we were quite moderate in modeling them, as not much data about them are available in the literature.

Navigation systems often report an RMSE after the head-to-MRI registration as a measure of the quality of registration. However, as seen in figure 5, this value does not tell about the navigation accuracy: with a small RMSE, the simulated average error can be high and vice versa. Hence, this measure should not be considered describing the reliability of the navigation system, as recognized also in the field of neurosurgery navigation [43, 57].

In our simulations, we omitted the errors arising from the relative placement of the tracking unit and the head and coil trackers, as the contribution of such errors for locating a single marker within the operating volume is likely very small [48, 58]. In addition, the generated Gaussian displacements in different steps of the coregistration process were isotropic, i.e. the error distributions were assumed similar in each direction. In practice, they can, however, be anisotropic [42, 58, 59], but the information in the literature about this topic is limited.

4.2. E-field errors

The E-field simulations showed that the within-method accuracies were quite similar across the E-field-navigation methods for all parameters studied (location, orientation, and magnitude of the E-field maximum). Line navigation had about twice as poor within-method location accuracy of about 3.5–5 mm as that of E-field navigations (1.5–3 mm), but its within-method orientation accuracy was about 1° and, thus, the best. When computing the between-method accuracy with the 4C BEM as a reference, the line navigation had the worst location accuracy (∼10 mm), with the accuracy increasing with more realistic head models (global and local sphere ∼8 mm; 1C/3C BEM ∼7 mm; 4C BEM ∼2 mm). Regarding the within-method accuracies, the surface-based registration led to approximately up to 1 mm and 1° better average accuracies as compared to the landmark-based registration; regarding the between-method accuracy, the differences between the registration methods were very small. The between-method accuracy of the E-field direction was the best with the BEMs (1.9°–7.6°) and the worst with the sphere approaches (up to about 15°); the between-method accuracy of the E-field magnitude was the best with the 4C BEM (∼5%) and the worst with the local sphere (∼25%; other methods ∼11%–18%). Here, the result with the 4C BEM is biased, as the same head model and parameters were used in reference and test computations. The 3C BEM result is also biased, as that model has more correct boundary

geometry information than the other models; in reality, all added detail would contain some error. Taking this into account, the difference of the errors in 3C and 1C BEM models is negligible; this supports the results of [28]. The comparison between the 1C BEM and sphere models is fair, as they all receive the same geometrical information. If one were to use a higher-detail model as the reference, the errors of the 4C BEM would likely increase slightly, and the differences between the 4C and simpler models would be smaller (see results in [24]).

The precisions of the peak E-field locations, orientations, and magnitudes were on average 0.6 mm, 0.6°, and 0.8%-points better with the surface-based than with the landmark-based registration. The precisions of the peak E-field locations got generally better with increasing realism in the head model, except that, interestingly, the precisions were worst with the local sphere and the 4C BEM. With 4C BEM, we see two possible explanations for this: first, the folded gyral geometry that is not included in other models may affect the local field profile so that a small shift in coil position has a larger effect. Further, the more focal field leads to smaller number of vertices averaged for the location metric, and thus higher sensitivity to such local effects.

With the local sphere method, the poor accuracies and precisions especially with Subject 2 are due to relatively big errors with two frontotemporal coil locations. Those locations were associated with a small size of the fitted sphere but flat underlying brain region. In this case, the cortical points under the coil center are relatively deep in the fitted sphere resulting in a weak E-field on those cortical points. Additionally, the cortical areas on the edges of the local region of interest are more superficial within the fitted sphere leading to a broad E-field profile and large variation for the location and orientation of the peak E-field. The effect of this is visible also for the peak E-field accuracies in supplementary figure S4 and supplementary table S1. Thus, it seems that the frontotemporal regions are not ideal for a local sphere approach at least with this realization.

As the E-field computation surface, we utilized the mid-cortical surface, which is folded according to the brain anatomy. However, some navigation systems utilize a smoothed surface, which can be created, for example, by shrinking the inner surface of the skull [28]. With the E-field computation space following the folded cortical anatomy, E-field maximum may easily jump from one gyrus to another (especially when the TMS coil is tilted or placed above a sulcus) regardless of the E-field computation model. As this is reality, we consider it beneficial to compute E-fields on a realistically folded cortical surface instead of a smoothed one, especially with higher-detail head models comprising folded conductivity compartments. The E-field simulations were carried out with head models of two subjects; the results across the two subjects were comparable. The individual effects in the E-field computations were mitigated by selecting 21 different locations based on electroencephalography electrode positions. In the future, corresponding simulations could be done with more subjects to confirm the level of E-field errors in a larger population.

A general assumption is that the TMS-induced activation occurs at the area of maximal E-field, and that is why the navigation systems show and record the information about the E-field maximum. However, the location of the peak E-field is not necessarily the place where the maximal activation occurs. In practice, the locus of activation is determined by the combined effect of the E-field profile and the cytoarchitectonics and the excitability state of the stimulated neuronal population [60–64]. This may be taken into account in future navigation systems.

We did not consider inaccuracies in the coil model, which can result from manufacturing errors, registration of the coil model to the physical coil, and the computational model of the coil. We applied a figure-of-eight coil model, approximated with 42 magnetic dipoles, which has been shown to compare well against a highly detailed coil model (relative cortical E-field error ∼1%) [35].

4.3. Needed nTMS accuracy and precision

Accuracy and precision may be of different importance in different TMS applications. One clinical application of TMS is preoperative mapping, which helps in the planning of neurosurgery and can improve surgical outcomes. In preoperative TMS mapping of the primary motor cortex (M1) or cortical speech areas, anatomical accuracy is evidently important; the required accuracy is achieved by nTMS with individual MRIs [65–68].

At the same time, the value of TMS as a *focal* (needs high accuracy and precision) brain stimulation technique in neuromodulation applications is not obvious. Currently, no clear need for millimeter-level accuracy in repetitive TMS (rTMS) is evident [69]. The majority of research and clinical guidelines for rTMS are about targeting a larger brain region, for example, the hand knob or the dorsolateral prefrontal cortex (DLPFC). Theoretically, navigation may benefit rTMS neuromodulation by providing accurate targeting of the desired brain region (anatomical guidance) and precise coil positioning, allowing consistent stimulation of the same target instead of many nearby targets, which may even inhibit each other [70]. A study on healthy subjects showed a more prominent effect of E-field-navigated low-frequency rTMS of M1 over non-navigated rTMS for both TMS phenomena and motor tasks [20]; the effect most probably resulted from the better precision of nTMS. Similarly, only a few studies have compared navigated versus non-navigated therapeutic rTMS in clinical populations [18, 71–73]. In depression [18] and pain

[71] studies, nTMS showed better therapeutic effect than non-nTMS, whereas, in a tinnitus study [72], no difference was found. In the study of Moreno-Ortega *et al* [73], a subregion of the DLPFC was determined based on functional connectivity and stimulated with nTMS, showing a greater therapeutic effect than non-nTMS. Thus, we can assume that accuracy at the level of the brain subregion is important when there is a clear optimal area for targeting. Moreover, if the TMS effect is sensitive to small changes in TMS parameters, also high precision is required. The level of nTMS accuracy and precision required in different applications needs further studies.

4.4. Ways to improve the accuracy and precision of navigated TMS

The accuracy and precision of nTMS may be improved from those of the presently used navigation pipelines. For example, at the cost of a slightly longer registration process, the quality of the surface-matching registration could be improved by collecting more scalp points [74]. Navigating the head placement with 3D laser scanning provides a head-tracker-free alternative that requires no digitizer tool [75]. Thus, such an approach could eliminate errors associated with the head tracker and the digitizer tool. At present, laser scanning, however, takes a considerable amount of time, which limits its real-time operation. To characterize registration errors during a TMS session, one can touch well-defined checkpoints on the head with the digitizer tool and compare the real position with the information presented by the navigation system [76]. Such a characterization may help in spotting errors due to a movement of the head tracker. The operation of nTMS can be automated when combining head-tracker-free navigation, hands-free control of the stimulation location and orientation with a robotic arm [77, 78] or multi-channel TMS [79, 80], and algorithms for automated guiding of TMS based on evoked electrophysiological responses [81–84]. Full automation would make nTMS more user-friendly and remove user-related error sources.

Bite-bar-based fiducials have been proposed as a way to increase the registration accuracy between an individual MRI and magnetoencephalography recordings [85]; a similar approach is applicable also in TMS. In surgical navigation applications, one may increase the quality of landmark-based registration by attaching to the head artificial fiducials visible in the MRI [86] or by invasive bone-implanted screws [87]; such approaches are, however, impractical for typical TMS. To minimize errors in the calculation of the E-field, we recommend realistic computational models instead of spherical head models, given that real-time implementation of realistic E-field modeling has already been demonstrated [24, 30].

5. Conclusion

We analyzed errors affecting TMS navigation. The accuracy and precision of the coil localization in the head-image coordinates as well as their effect in the E-field estimation depend on the navigation methods. We suggest utilizing the surface-based approach for head-to-MRI registration and realistic models for E-field computations to enable reliable TMS navigation.

Data availability statement

The data generated and/or analysed during the current study are not publicly available for legal/ethical reasons but are available from the corresponding author on reasonable request.

Acknowledgments

We acknowledge funding from the Finnish Cultural Foundation, Academy of Finland (Decisions Nos. 294625, 306845, and 327326), Instrumentarium Science Foundation, and European Research Council (ERC Synergy) under the European Union's Horizon 2020 research and innovation programme (Connect-ToBrain; Grant Agreement No. 810377). M.N. and P.N. were supported by the Basic Research Program of HSE University, P.N. was supported by Aalto AScI Visiting Researcher Programme, and M.N was supported by the NIH Brain Initiative Biology and Biophysics of Neural Stimulation and Recording Technologies (1R01NS112183-01A1). In addition, we would like to thank Science-IT at Aalto University School of Science for computational resources.

Declarations of interest

R.J.I. has been advisor and is a minority shareholder of Nexstim Plc. The other authors declare no competing interests.

ORCID iDs

Aino E Nieminen https://orcid.org/0000-0002-6841-7043
Jaakko O Nieminen https://orcid.org/0000-0002-7826-3519
Pavel Novikov https://orcid.org/0000-0003-4102-1580
Maria Nazarova https://orcid.org/0000-0001-5347-5948
Selja Vaalto https://orcid.org/0000-0002-7326-4766
Vadim Nikulin https://orcid.org/0000-0001-6082-3859
Risto J Ilmoniemi https://orcid.org/0000-0002-3340-2618

References

[1] Barker A T, Jalinous R and Freeston I L 1985 Non-invasive magnetic stimulation of human motor cortex *Lancet* **325** 1106–7

[2] Ilmoniemi R J, Ruohonen J and Karhu J 1999 Transcranial magnetic stimulation—a new tool for functional imaging of the brain *Crit. Rev. Biomed. Eng.* **27** 241–84

[3] Herwig U, Schönfeldt-Lecuona C, Wunderlich A P, von Tiesenhausen C, Thielscher A, Walter H and Spitzer M 2001 The navigation of transcranial magnetic stimulation *Psychiatry Res. Neuroimaging* **108** 123–31

[4] Ruohonen J and Karhu J 2010 Navigated transcranial magnetic stimulation *Neurophysiol. Clin.* **40** 7–17

[5] Hannula H and Ilmoniemi R J 2017 Basic principles of navigated TMS *Navigated Transcranial Magnetic Stimulation in Neurosurgery* ed S M Krieg (Cham: Springer) pp 3–29

[6] Comeau R 2014 Neuronavigation for transcranial magnetic stimulation *Transcranial Magnetic Stimulation* ed A Rotenberg, J C Horvath and A Pascual-Leone (New York: Humana Press) pp 31–56

[7] Lefaucheur J-P 2010 Why image-guided navigation becomes essential in the practice of transcranial magnetic stimulation *Neurophysiol. Clin.* **40** 1–5

[8] Gugino L D, Romero R J, Aglio L, Titone D, Ramirez M, Pascual-Leone A, Grimson E, Weisenfeld N, Kikinis R and Shenton M-E 2001 Transcranial magnetic stimulation coregistered with MRI: a comparison of a guided versus blind stimulation technique and its effect on evoked compound muscle action potentials *Clin. Neurophysiol.* **112** 1781–92

[9] Julkunen P, Säisänen L, Danner N, Niskanen E, Hukkanen T, Mervaala E and Könönen M 2009 Comparison of navigated and non-navigated transcranial magnetic stimulation for motor cortex mapping, motor threshold and motor evoked potentials *Neuroimage* **44** 790–5

[10] Lioumis P, Kičić D, Savolainen P, Mäkelä J P and Kähkönen S 2009 Reproducibility of TMS-evoked EEG responses *Hum. Brain Mapp.* **30** 1387–96

[11] Siebner H R *et al* 2009 Consensus paper: combining transcranial stimulation with neuroimaging *Brain Stimul.* **2** 58–80

[12] Krings T, Buchbinder B R, Butler W E, Chiappa K H, Jiang H J, Rosen B R and Cosgrove G R 1997 Stereotactic transcranial magnetic stimulation: correlation with direct electrical cortical stimulation *Neurosurgery* **41** 1319–26

[13] Krieg S M, Shiban E, Buchmann N, Gempt J, Foerschler A, Meyer B and Ringel F 2012 Utility of presurgical navigated transcranial magnetic brain stimulation for the resection of tumors in eloquent motor areas *J. Neurosurg.* **116** 994–1001

[14] Nazarova M, Novikov P, Ivanina E, Kozlova K, Dobrynina L and Nikulin V V 2021 Mapping of multiple muscles with transcranial magnetic stimulation: absolute and relative test–retest reliability *Hum. Brain Mapp.* **42** 2508–28

[15] Picht T *et al* 2013 A comparison of language mapping by preoperative navigated transcranial magnetic stimulation and direct cortical stimulation during awake surgery *Neurosurgery* **72** 808–19

[16] Lioumis P, Zhdanov A, Mäkelä N, Lehtinen H, Wilenius J, Neuvonen T, Hannula H, Deletis V, Picht T and Mäkelä J P 2012 A novel approach for documenting naming errors induced by navigated transcranial magnetic stimulation *J. Neurosci. Methods* **204** 349–54

[17] Lefaucheur J-P, Brugières P, Ménard-Lefaucheur I, Wendling S, Pommier M and Bellivier F 2007 The value of navigation-guided rTMS for the treatment of depression: an illustrative case *Neurophysiol. Clin.* **37** 265–71

[18] Fitzgerald P B, Hoy K, McQueen S, Maller J J, Herring S, Segrave R, Bailey M, Been G, Kulkarni J and Daskalakis Z J 2009 A randomized trial of rTMS targeted with MRI based neuro-navigation in treatment-resistant depression *Neuropsychopharmacology* **34** 1255–62

[19] Ayache S S, Ahdab R, Chalah M A, Farhat W H, Mylius V, Goujon C, Sorel M and Lefaucheur J-P 2016 Analgesic effects of navigated motor cortex rTMS in patients with chronic neuropathic pain *Eur. J. Pain* **20** 1413–22

[20] Bashir S, Edwards D and Pascual-Leone A 2011 Neuronavigation increases the physiologic and behavioral effects of low-frequency rTMS of primary motor cortex in healthy subjects *Brain Topogr.* **24** 54–64

[21] West J B and Maurer C R 2004 Designing optically tracked instruments for image-guided surgery *IEEE Trans. Med. Imaging* **23** 533–45

[22] Maurer C R, Rohlfing T, Dean D, West J B, Rueckert D, Mori K, Shahidi R, Martin D P, Heilbrun M P and Maciunas R J 2002 Sources of error in image registration for cranial image-guided neurosurgery *Advanced Techniques in Image-Guided Brain and Spine Surgery* ed I M Germano (New York: Thieme) pp 10–36

[23] Wang M N and Song Z J 2011 Classification and analysis of the errors in neuronavigation *Neurosurgery* **68** 1131–43

[24] Stenroos M and Koponen L M 2019 Real-time computation of the TMS-induced electric field in a realistic head model *Neuroimage* **203** 116159

[25] Gomez L J, Dannhauer M, Koponen L M and Peterchev A V 2020 Conditions for numerically accurate TMS electric field simulation *Brain Stimul.* **13** 157–66

[26] Sollmann N, Goblirsch-Kolb M F, Ille S, Butenschoen V M, Boeckh-Behrens T, Meyer B, Ringel F and Krieg S M 2016 Comparison between electric-field-navigated and line-navigated TMS for cortical motor mapping in patients with brain tumors *Acta Neurochir.* **158** 2277–89

[27] Heller L and van Hulsteyn D B 1992 Brain stimulation using electromagnetic sources: theoretical aspects *Biophys. J.* **63** 129–38

[28] Nummenmaa A, Stenroos M, Ilmoniemi R J, Okada Y C, Hämäläinen M S and Raij T 2013 Comparison of spherical and realistically shaped boundary element head models for transcranial magnetic stimulation navigation *Clin. Neurophysiol* **124** 1995–2007

[29] Laakso I and Hirata A 2012 Fast multigrid-based computation of the induced electric field for transcranial magnetic stimulation *Phys. Med. Biol.* **57** 7753–65

[30] Daneshzand M, Makarov S N, de Lara L I N, Guerin B, McNab J, Rosen B R, Hämäläinen M S, Raij T and Nummenmaa A 2021 Rapid computation of TMS-induced E-fields using a dipole-based magnetic stimulation profile approach *Neuroimage* **237** 118097

[31] Saturnino G B, Thielscher A, Madsen K H, Knösche T R and Weise K 2019 A principled approach to conductivity uncertainty analysis in electric field calculations *Neuroimage* **188** 821–34

[32] Nielsen J D, Madsen K H, Puonti O, Siebner H R, Bauer C, Madsen C G, Saturnino G B and Thielscher A 2018 Automatic skull segmentation from MR images for realistic volume conductor models of the head: assessment of the state-of-the-art *Neuroimage* **174** 587–98

[33] Rashed E A, Gomez-Tames J and Hirata A 2021 Influence of segmentation accuracy in structural MR head scans on electric field computation for TMS and tES *Phys. Med. Biol.* **66** 064002

[34] Mikkonen M and Laakso I 2019 Effects of posture on electric fields of non-invasive brain stimulation *Phys. Med. Biol.* **64** 065019

[35] Stenroos M and Koponen L M 2021 Effect of coil model detail on computed electric field in TMS *Int. J. Bioelectromagn.* **23** 15/1–5

[36] Schönfeldt-Lecuona C, Thielscher A, Freudenmann R W, Kron M, Spitzer M and Herwig U 2005 Accuracy of stereotaxic positioning of transcranial magnetic stimulation *Brain Topogr.* **17** 253–9

[37] Souza V H, Matsuda R H, Peres A S C, Amorim P H J, Moraes T F, Silva J V L and Baffa O 2018 Development and characterization of the InVesalius Navigator software for navigated transcranial magnetic stimulation *J. Neurosci. Methods* **309** 109–20

[38] Spetzger U, Hubbe U, Struffert T, Reinges M H T, Krings T, Krombach G A, Zentner J, Gilsbach J M and Stiehl H S 2002 Error analysis in cranial neuronavigation *Minim. Invasive Neurosurg.* **45** 6–10
[39] Widmann G, Schullian P, Ortler M and Bale R 2012 Frameless stereotactic targeting devices: technical features, targeting errors and clinical results *Int. J. Med. Robot. Comput. Assist. Surg.* **8** 1–16
[40] Schmidt S, Bathe-Peters R, Fleischmann R, Rönnefarth M, Scholz M and Brandt S A 2015 Nonphysiological factors in navigated TMS studies; confounding covariates and valid intracortical estimates *Hum. Brain Mapp.* **36** 40–49
[41] World Medical Association 2013 World Medical Association Declaration of Helsinki: Ethical principles for medical research involving human subjects *JAMA* **310** 2191–4
[42] Shamir R R, Joskowicz L and Shoshan Y 2012 Fiducial optimization for minimal target registration error in image-guided neurosurgery *IEEE Trans. Med. Imaging* **31** 725–37
[43] Shamir R R, Joskowicz L, Spektor S and Shoshan Y 2009 Localization and registration accuracy in image guided neurosurgery: a clinical study *Int. J. Comput. Assist. Radiol. Surg.* **4** 45–52
[44] Omara A I, Wang M, Fan Y and Song Z 2013 Anatomical landmarks for point-matching registration in image-guided neurosurgery *Int. J. Med. Robot. Comput. Assist. Surg.* **10** 55–64
[45] Umeyama S 1991 Least-squares estimation of transformation parameters between two point patterns *IEEE Trans. Pattern Anal. Mach. Intell.* **13** 376–80
[46] Besl P J and McKay N D 1992 A method for registration of 3D shapes *IEEE Trans. Pattern Anal. Mach. Intell.* **14** 239–56
[47] Torfeh T, Hammoud R, Perkins G, McGarry M, Aouadi S, Celik A, Hwang K-P, Stancanello J, Petric P and Al-Hammadi N 2016 Characterization of 3D geometric distortion of magnetic resonance imaging scanners commissioned for radiation therapy planning *Magn. Reson. Imaging* **34** 645–53
[48] Wiles A D, Thompson D G and Frantz D D 2004 Accuracy assessment and interpretation for optical tracking systems *Proc. SPIE* **5367** 421–32
[49] Möller T and Trumbore B 1997 Fast, minimum storage ray-triangle intersection *J. Graph. Tools* **2** 21–28
[50] Plonsey R 1972 Capability and limitations of electrocardiography and magnetocardiography *IEEE Trans. Biomed. Eng.* **BME-19** 239–44
[51] Sarvas J 1987 Basic mathematical and electromagnetic concepts of the biomagnetic inverse problem *Phys. Med. Biol.* **32** 11–22
[52] Stenroos M and Sarvas J 2012 Bioelectromagnetic forward problem: isolated source approach revis(it)ed *Phys. Med. Biol.* **57** 3517–35
[53] Stenroos M and Nummenmaa A 2016 Incorporating and compensating cerebrospinal fluid in surface-based forward models of magneto- and electroencephalography *PLoS One* **11** e0159595
[54] Hämäläinen M S and Sarvas J 1989 Realistic conductivity geometry model of the human head for interpretation of neuromagnetic data *IEEE Trans. Biomed. Eng.* **36** 165–71
[55] Thielscher A, Opitz A and Windhoff M 2011 Impact of the gyral geometry on the electric field induced by transcranial magnetic stimulation *Neuroimage* **54** 234–43
[56] Fitzpatrick J M, West J B and Maurer C R 1998 Predicting error in rigid-body point-based registration *IEEE Trans. Med. Imaging* **17** 694–702
[57] Labadie R F, Davis B M and Fitzpatrick J M 2005 Image-guided surgery: what is the accuracy? *Curr. Opin. Otolaryngol. Head Neck Surg.* **13** 27–31
[58] Khadem R, Yeh C C, Sadeghi-Tehrani M, Bax M R, Johnson J A, Welch J N, Wilkinson E P and Shahidi R 2000 Comparative tracking error analysis of five different optical tracking systems *Comput. Aided Surg.* **5** 98–107
[59] Wiles A D, Likholyot A, Frantz D D and Peters T M 2008 A statistical model for point-based target registration error with anisotropic fiducial localizer error *IEEE Trans. Med. Imaging* **27** 378–90
[60] Weise K, Numssen O, Thielscher A, Hartwigsen G and Knösche T R 2020 A novel approach to localize cortical TMS effects *Neuroimage* **209** 116486
[61] Kataja J, Soldati M, Matilainen N and Laakso I 2021 A probabilistic transcranial magnetic stimulation localization method *J. Neural Eng.* **18** 0460f3
[62] Mutanen T P, Souza V H, Nieminen J O and Ilmoniemi R J 2021 On the effective resolution of TMS, its tradeoff with signal-to-noise ratio, and the experimental implications *Int. J. Bioelectromagn.* **23** 13/1–4
[63] Aberra A S, Wang B, Grill W M and Peterchev A V 2020 Simulation of transcranial magnetic stimulation in head model with morphologically-realistic cortical neurons *Brain Stimul.* **13** 175–89
[64] Siebner H R *et al* 2022 Transcranial magnetic stimulation of the brain: what is stimulated?—a consensus and critical position paper *Clin. Neurophysiol.* **140** 59–97
[65] Takahashi S, Vajkoczy P and Picht T 2013 Navigated transcranial magnetic stimulation for mapping the motor cortex in patients with Rolandic brain tumors *Neurosurg. Focus* **34** E3
[66] Lefaucheur J-P and Picht T 2016 The value of preoperative functional cortical mapping using navigated TMS *Neurophysiol. Clin.* **46** 125–33
[67] Ille S *et al* 2015 Combined noninvasive language mapping by navigated transcranial magnetic stimulation and functional MRI and its comparison with direct cortical stimulation *J. Neurosurg.* **123** 212–25
[68] Ille S *et al* 2015 Impairment of preoperative language mapping by lesion location: a functional magnetic resonance imaging, navigated transcranial magnetic stimulation, and direct cortical stimulation study *J. Neurosurg.* **123** 314–24
[69] Lefaucheur J-P *et al* 2020 Evidence-based guidelines on the therapeutic use of repetitive transcranial magnetic stimulation (rTMS): an update (2014–2018) *Clin. Neurophysiol.* **131** 474–528
[70] Sohn Y H and Hallett M 2004 Disturbed surround inhibition in focal hand dystonia *Ann. Neurol.* **56** 595–9
[71] Ahdab R, Ayache S S, Brugières P, Goujon C and Lefaucheur J-P 2010 Comparison of "standard" and "navigated" procedures of TMS coil positioning over motor, premotor and prefrontal targets in patients with chronic pain and depression *Neurophysiol. Clin.* **40** 27–36
[72] Sahlsten H *et al* 2019 Neuronavigated versus non-navigated repetitive transcranial magnetic stimulation for chronic tinnitus: a randomized study *Trends Hear* **23** 1–14
[73] Moreno-Ortega M, Kangarlu A, Lee S, Perera T, Kangarlu J, Palomo T, Glasser M F and Javitt D C 2020 Parcel-guided rTMS for depression *Transl. Psychiatry* **10** 283
[74] Noirhomme Q, Ferrant M, Vandermeeren Y, Olivier E, Macq B and Cuisenaire O 2004 Registration and real-time visualization of transcranial magnetic stimulation with 3-D MR images *IEEE Trans. Biomed. Eng.* **51** 1994–2005
[75] Hironaga N, Kimura T, Mitsudo T, Gunji A and Iwata M 2019 Proposal for an accurate TMS-MRI co-registration process via 3D laser scanning *Neurosci. Res.* **144** 30–39
[76] Widmann G, Stoffner R and Bale R 2009 Errors and error management in image-guided craniomaxillofacial surgery *Oral Surg. Oral Med. Oral Pathol. Oral Radiol. Endodontol.* **107** 701–15
[77] Lancaster J L, Narayana S, Wenzel D, Luckemeyer J, Roby J and Fox P 2004 Evaluation of an image-guided, robotically positioned transcranial magnetic stimulation system *Hum. Brain Mapp.* **22** 329–40
[78] Lebossé C, Renaud P, Bayle B, de Mathelin M, Piccin O and Foucher J 2007 A robotic system for automated image-guided transcranial magnetic stimulation *IEEE/NIH Life Science Systems and Applications Workshop* pp 55–58

[79] Koponen L M, Nieminen J O and Ilmoniemi R J 2018 Multi-locus transcranial magnetic stimulation—theory and implementation *Brain Stimul.* **11** 849–55
[80] Nieminen J O *et al* 2022 Multi-locus transcranial magnetic stimulation system for electronically targeted brain stimulation *Brain Stimul.* **15** 116–24
[81] Meincke J, Hewitt M, Batsikadze G and Liebetanz D 2016 Automated TMS hotspot-hunting using a closed loop threshold-based algorithm *Neuroimage* **124** 509–17
[82] Harquel S, Diard J, Raffin E, Passera B, Dall'Igna G, Marendaz C, David O and Chauvin A 2017 Automatized set-up procedure for transcranial magnetic stimulation protocols *Neuroimage* **153** 307–18
[83] Tervo A E, Metsomaa J, Nieminen J O, Sarvas J and Ilmoniemi R J 2020 Automated search of stimulation targets with closed-loop transcranial magnetic stimulation *Neuroimage* **220** 117082
[84] Tervo A E, Nieminen J O, Lioumis P, Metsomaa J, Souza V H, Sinisalo H, Stenroos M, Sarvas J and Ilmoniemi R J 2022 Closed-loop optimization of transcranial magnetic stimulation with electroencephalography feedback *Brain Stimul.* **15** 523–31
[85] Adjamian P, Barnes G R, Hillebrand A, Holliday I E, Singh K D, Furlong P L, Harrington E, Barclay C W and Route P J G 2004 Co-registration of magnetoencephalography with magnetic resonance imaging using bite-bar-based fiducials and surface-matching *Clin. Neurophysiol.* **115** 691–8
[86] Pfisterer W K, Papadopoulos S, Drumm D A, Smith K and Preul M C 2008 Fiducial versus nonfiducial neuronavigation registration assessment and consideration of accuracy *Oper. Neurosurg.* **62** 201–8
[87] Mascott C R, Sol J-C, Bousquet P, Lagarrigue J, Lazorthes Y and Lauwers-Cances V 2006 Quantification of true *in vivo* (application) accuracy in cranial image-guided surgery: influence of mode of patient registration *Oper. Neurosurg.* **59** 146–56